Theses

5-12-2017

Multi-Domain Spectral Methods for Data Reduction in Numerical Relativity Simulations

Brian A. Caimano
bac5933@rit.edu

R·I·T

Multi-Domain Spectral Methods for Data Reduction in Numerical Relativity Simulations

by

Brian A Caimano

A Thesis Submitted in Partial Fulfillment of the Requirements for the Degree of Master of Science in Applied and Computational Mathematics

College of Science
School of Mathematical Sciences
Center for Computational Relativity and Gravitation

Rochester Institute of Technology
Rochester, NY
May 12, 2017

Committee Approval:

Matthew J. Hoffman, Ph.D.   Date
School of Mathematical Sciences
Director of Graduate Programs, SMS

Joshua A. Faber, Ph.D.   Date
School of Mathematical Sciences
Thesis Advisor

Yosef Zlochower, Ph.D.   Date
School of Mathematical Sciences
Committee Member

Anthony A. Harkin, Ph.D.   Date
School of Mathematical Sciences
Committee Member

This thesis is dedicated to my parents, Roger and Jonatha, for always letting me go my own way and having the faith that I would succeed.

Abstract

Numerical relativity simulations of binary black hole inspiraling and mergers are computationally costly and storage requirements can quickly become unmanageable. By implementing a multi-domain spectral method we are able to more efficiently store metric component data when increased time resolution is desired over increased spatial metric resolution. Within the framework of a binary black hole system, multi-domain spectral methods work well using two different domain sets, one centered on each black hole, so they are able to absorb the singular behavior at each black hole's center. There is no difficulty in transferring quantities from one domain to another, or splitting the source function across two different domains, but there is no a priori choice for the relative weighting function to split a metric component. Here, we investigate what breakdown yields the highest accuracy.

Contents

List of Figures

List of Tables

Chapter 1

Introduction

We have recently passed the century mark for Einstein's publication of his general theory of relativity [7]. This theory has provided us with the framework to model gravity on scales ranging from terrestrial to cosmological. To date, the general relativistic gravitational model has passed numerous test across multiple length scales. This theory has allowed modeling of large-scale cosmological structures, astrophysical objects such as black holes, neutron stars and other compact bodies, as well as more everyday applications such as GPS systems. Further evidence of the experimental accuracy of general relativity occurred in September 2015, a century after the fundamental predictions of Einstein and Schwarzschild, when the first direct detection of gravitational waves occured. This was the first direct observation of a binary black hole system merging to form a single black hole, in accordance with the predictions of general relativity for the nonlinear dynamics of highly disturbed black holes [1].

In an effort to construct and study more general solutions to the field equations by approximately solving the Einstein equations numerically, the field of numerical relativity was born. The first decomposition of spacetime into separate space and time components was published by Richard Arnowitt, Stanley Deser, and Charles W. Misner in the late 1950s in what has become known as the ADM formalism [2]. Unfortunately, in its simplest form, the so-called 3+1 split (representing the spatial and time dimensions, respectively) is numerically unstable and not useful for simulating general configurations in time. Current numerical efforts most commonly employ one of two particular reformulations of Einstein's equations: the generalized harmonic gauge [15] or the BSSN (Barmgarte-Shapiro-Shibata-Nakamura) formalisms [3].

Numerical methods to find solutions for valid initial data in general relativity seek the solution of the Hamiltonian constraint [9]

$$\Delta\psi + \frac{1}{8}K^{ab}K_{ab}\psi^{-7} = 0, \qquad (1.1)$$

with boundary conditions $\psi \to 1$ and $r \to \infty$ where the physical extrinsic curvature, $\hat{K}^{ab}$, is scaled by a conformal factor, ψ, to produce the conformal extrinsic curvature, K^{ab}, such that

$$K^{ab} = \psi^2 \hat{K}^{ab}. \qquad (1.2)$$

A solution known to work for black hole spacetime configurations, the Bowen-York solution to the momentum constraints, K_{ab}, for two black holes, with momentums P_1 and P_2, and spins S_1 and S_2, is given by

$$K_{ab} = \sum_{k=1}^{2} \frac{3}{2r_k^2} \left[P_k^a n_k^b + P_k^b n_k^a - (\gamma^{ab} - n_k^a n_k^b)(P_k n_k) \right]$$
$$+ \frac{3}{r_k^3} \left[(S_k \times n_k)^a n_k^b + (S_k \times n_k)^b n_k^a \right], \qquad (1.3)$$

where

$$r_k = \sqrt{(x \pm b)^2 + y^2 + z^2} \qquad (1.4)$$

is the coordinate distance to black holes $k \in \{1, 2\}$ located at the points $(\pm b, 0, 0)$, n_k is the radial unit normal vector given by

$$n_k = \frac{x^a}{r_k} \qquad (1.5)$$

and γ is the conformal three-metric.

Binary black hole simulations, including those performed at RIT by researchers in the Center for Computational Relativity and Gravitation (CCRG), are most often performed using Eulerian evolution schemes in which a grid of spatial coordinates is laid down, describing the set of points where various quantities like the values of the spacetime metric tensor are calculated via the partial differential equation (1.1). These calculations, which require high spatial resolution near the respective black holes, as well as a large numerical domain to capture the asymptotic behavior of the gravitational radiation produced by the binary system, typically utilize adaptive mesh

refinement using a sequence of nested, logically rectangular meshes on which the partial differential equation is discretized [4]. This technique allows for the adaptation of precision for areas of the model that exhibit dynamic and/or multi-scale behavior. For our work on initial data, we use `Carpet`, an adaptive mesh refinement and multi-patch driver [14], via code found at `http://einsteintoolkit.org/` [10]. These types of problems have extreme data storage requirements since each level of refinement is often quite large, potentially including millions of grid cells, with up to 15 levels of refinement being called upon for the highest resolution simulations [11]. To combat this we look for methods to store data more efficiently, preserving the vast majority of the information content from a simulation while reducing the overall storage requirements.

In this thesis, we investigate methods of storing spacetime metric component data of a binary black hole system on multi-domain spherical grids, and using spectral methods to reconstruct the field for use in post-processing applications such as radiative transfer [13]. We begin by constructing a multi-domain grid, inputting known values of a function at the collocation points required to perform a spectral decomposition, and constructing a grid of spectrally expanded values in order to verify the accuracy of the method. We then construct a Cartesian grid of known data, interpolate those values onto the multi-domain grid, and analyze the error introduced by the interpolation routine. Lastly, we construct two multi-domain grids, one centered at each black hole, interpolate numerically derived data to the grid, split the metric values between the two multi-domain grids, then reconstruct the original metric and analyze the resulting error.

Chapter 2

Multi-Domain Grids

Using the `LORENE` numerical libraries [8], we construct a multi-domain grid as described in [5], consisting of an inner spherical domain, intermediate annular domains, and an exterior domain extending to spatial infinity. We divide $\mathbb{R}^3$ into $\mathcal{N}$ domains $(\mathcal{D}_l)_{0 \leq l \leq \mathcal{N}-1}$ where $\mathcal{N} \geq 2$. Let us denote by $\mathcal{S}_l$ the boundary surface between the domains $\mathcal{D}_l$ and $\mathcal{D}_{l+1}$. $\mathcal{D}_0$ is simply connected and its boundary is $\mathcal{S}_0$; we call it the nucleus. For $1 \leq l \leq \mathcal{N} - 2$, the inner boundary of $\mathcal{D}_l$ is $\mathcal{S}_{l-1}$ and outer boundary $\mathcal{S}_l$. The infinite domain, $\mathcal{D}_{\mathcal{N}-1}$, has inner boundary $\mathcal{S}_{\mathcal{N}-2}$ and extends to spatial infinity [5]. See Figure 2.1 on page 7 for an example.

2.1 Inner Domain

We begin by constructing the mapping

$$[0, 1] \times [0, \pi] \times [0, 2\pi) \to \mathcal{D}_0, \; (\xi, \theta', \phi') \mapsto (r, \theta, \phi), \tag{2.1}$$

where $\xi = 0$ corresponds to the origin [5]. We take the form of mapping 2.1 to be

$$r = R_0(\xi, \theta', \phi'), \tag{2.2}$$
$$\theta = \theta', \tag{2.3}$$
$$\phi = \phi', \tag{2.4}$$

where $R_0(\xi, \theta, \phi)$ satisfies

$$R_0(1, \theta, \phi) = \mathcal{S}_0(\theta, \phi) \tag{2.5}$$

since the domain boundaries coincide with $\xi = 1$ [5]. So R_0 is defined as

$$R_0(\xi, \theta, \phi) = \alpha_0[\xi + A_0(\xi)F_0(\theta, \phi) + B_0(\xi)G_0(\theta, \phi)], \qquad (2.6)$$

where

$$A_0(\xi) = 3\xi^4 - 2\xi^6, \qquad (2.7)$$
$$B_0(\xi) = (5\xi^3 - 3\xi^5)/2, \qquad (2.8)$$

A_0 being an even polynomial and B_0 being an odd polynomial[5] and

$$\alpha_0 = S_0(\theta, \phi). \qquad (2.9)$$

The functions $F_0(\theta, \phi)$ and $G_0(\theta, \phi)$ allow the inner domain to be spheroidal in geometry since it allows for variation in the radial functions $A_0(\xi)$ and $B_0(\xi)$ with respect to the angular variables. We are using spherical mappings so we take $F_0(\theta, \phi) = G_0(\theta, \phi) = 0$.

2.2   Intermediate Domains

Domains $\mathcal{D}_l$, such that $1 \leq l \leq \mathcal{N} - 2$, are intermediate domains and are constructed with the mapping

$$[-1, 1] \times [0, \pi] \times [0, 2\pi) \to \mathcal{D}_l, \ (\xi, \theta', \phi') \mapsto (r, \theta, \phi) \qquad (2.10)$$

such that the form of mapping 2.10 is

$$r = R_l(\xi, \theta', \phi'), \qquad (2.11)$$
$$\theta = \theta', \qquad (2.12)$$
$$\phi = \phi', \qquad (2.13)$$

where $R_l(\xi, \theta, \phi)$ satisfies

$$R_l(-1, \theta, \phi) = \mathcal{S}_{l-1}(\theta, \phi), \qquad (2.14)$$
$$R_l(1, \theta, \phi) = \mathcal{S}_l(\theta, \phi), \qquad (2.15)$$

so that the inner (outer) boundary of D_l is defined by $\xi = -1$ ($\xi = 1$) [5]. R_l is defined as

$$R_l(\xi, \theta, \phi) = \alpha_l[\xi + A_l(\xi)F_l(\theta, \phi) + B_l(\xi)G_l(\theta, \phi)] + \beta_l, \qquad (2.16)$$

where

$$A_l(\xi) = (\xi^3 - 3\xi + 2)/4, \tag{2.17}$$
$$B_l(\xi) = (-\xi^3 + 3\xi + 2)/4 \tag{2.18}$$

and

$$\alpha_l = \frac{S_{l+1}(\theta, \phi) - S_l(\theta, \phi)}{2}, \tag{2.19}$$
$$\beta_l = \frac{S_{l+1}(\theta, \phi) + S_l(\theta, \phi)}{2} \tag{2.20}$$

are defined from S_{l+1} and S_l [5]. As with the inner domain, we take $F_0(\theta, \phi) = G_0(\theta, \phi) = 0$.

2.3 Infinite Domain

The external domain, $\mathcal{D}_{\text{ext}} \equiv \mathcal{D}_{\mathcal{N}-1}$, is the outermost domain with inner boundary $S_{\text{ext}} \equiv S_{\mathcal{N}-2}$, which extends to infinity and has the following mapping:

$$[-1, 1] \times [0, \pi] \times [0, 2\pi) \to \mathcal{D}_{\text{ext}}, \ (\xi, \theta', \phi') \mapsto (r, \theta, \phi) \tag{2.21}$$

such that the form of mapping 2.21 is

$$r = \frac{1}{U(\xi, \theta', \phi')}, \tag{2.22}$$
$$\theta = \theta', \tag{2.23}$$
$$\phi = \phi', \tag{2.24}$$

where

$$U(\xi, \theta, \phi) = \alpha_{\text{ext}}[\xi + A_{\text{ext}}(\xi)F_{\text{ext}}(\theta, \phi) - 1] \tag{2.25}$$

is a smooth function that satisfies

$$U(-1, \theta, \phi) = S_{\text{ext}}(\theta, \phi)^{-1}, \tag{2.26}$$
$$U(1, \theta, \phi) = 0 \tag{2.27}$$
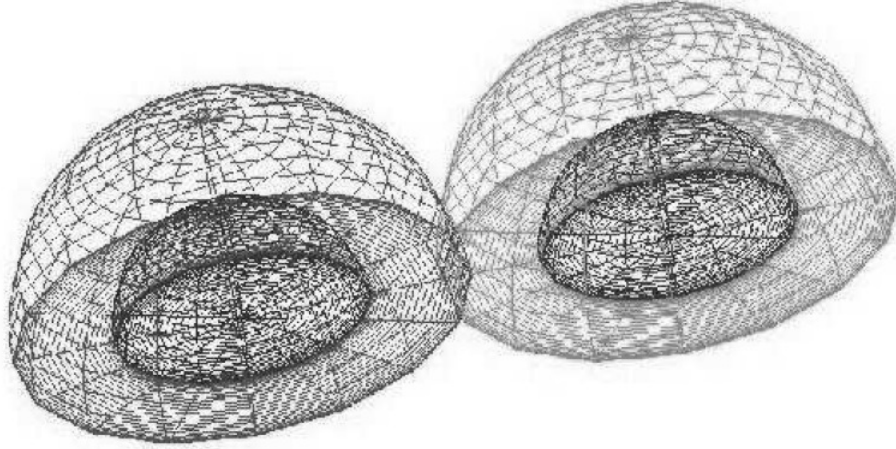
Figure 2.1: Example of multi-domain grids.

and $A_{\text{ext}}(\xi) \equiv A_l(\xi)$, as given in section 2.2 [5]. α_{ext} and F_{ext} are

$$\alpha_{\text{ext}} = \frac{S_{\text{ext}}(\theta, \phi)^{-1}}{-2 + F_{\text{ext}}(\theta, \phi)}, \qquad (2.28)$$

$$F_{\text{ext}}(\theta, \phi) \leq 0. \qquad (2.29)$$

Condition (2.29) ensures a non-singular mapping [5].

Chapter 3

Data Approximation

We approximate metric data from a finite Cartesian grid generated by the `Cactus` routines within the `EinsteinToolkit` to the newly constructed multi-domain grid. We utilize trilinear and tricubic approximation routines and then compare the resultant error data to expected error trends.

3.1 Cubic Interpolation

We first define the distance from the target coordinate, (x, y, z), to the next smaller coordinate with known data, (x_0, y_0, z_0), along each axis, so we have

$$x_d = \frac{(x - x_0)}{(x_1 - x_0)}, \tag{3.1}$$

$$y_d = \frac{(y - y_0)}{(y_1 - y_0)}, \tag{3.2}$$

$$z_d = \frac{(z - z_0)}{(z_1 - z_0)}. \tag{3.3}$$

Let $V[x_i, y_j, z_k]$ be the function value at (x_i, y_j, z_k) for $i, j, k \in [-1, 2]$. Interpolating first along the x-axis, we have

$$
\begin{aligned}
c_{jk} = V(x_{-1}, y_j, z_k) & \frac{x_d(x_d - 1)(x_d - 2)}{-6} \\
+ V(x_0, y_j, z_k) & \frac{(x_d + 1)(x_d - 1)(x_d - 2)}{2} \\
+ V(x_1, y_j, z_k) & \frac{(x_d + 1)x_d(x_d - 2)}{-2} \\
+ V(x_2, y_j, z_k) & \frac{(x_d + 1)x_d(x_d - 1)}{6},
\end{aligned}
\tag{3.4}
$$

where $j, k \in [-1, 2]$. Next we interpolate along the y-axis

$$
\begin{aligned}
c_i = c_{-1,i} & \frac{y_d(y_d - 1)(y_d - 2)}{-6} \\
+ c_{0,i} & \frac{(y_d + 1)(y_d - 1)(y_d - 2)}{2} \\
+ c_{1,i} & \frac{(y_d + 1)y_d(y_d - 2)}{-2} \\
+ c_{2,i} & \frac{(y_d + 1)y_d(y_d - 1)}{6},
\end{aligned}
\tag{3.5}
$$

for $i \in [-1, 2]$. We then interpolate along the z-axis

$$
\begin{aligned}
c = c_{-1} & \frac{z_d(z_d - 1)(z_d - 2)}{-6} \\
+ c_0 & \frac{(z_d + 1)(z_d - 1)(z_d - 2)}{2} \\
+ c_1 & \frac{(z_d + 1)z_d(z_d - 2)}{-2} \\
+ c_2 & \frac{(z_d + 1)z_d(z_d - 1)}{6},
\end{aligned}
\tag{3.6}
$$

where c is the approximate function value at the target coordinate.

3.2 Linear Interpolation

We again define the distance from the target coordinate, (x, y, z), to the next smaller coordinate with known data, (x_0, y_0, z_0), along each axis, so we have

$$x_d = \frac{(x - x_0)}{(x_1 - x_0)}, \tag{3.7}$$

$$y_d = \frac{(y - y_0)}{(y_1 - y_0)}, \tag{3.8}$$

$$z_d = \frac{(z - z_0)}{(z_1 - z_0)}. \tag{3.9}$$

Let $V[x_i, y_j, z_k]$ be the function value at (x_i, y_j, z_k) for $i, j, k \in [0, 1]$. Interpolating first along the x-axis, we have

$$c_{jk} = V[x_0, y_j, z_k](1 - x_d) + V[x_1, y_j, z_k]x_d, \tag{3.10}$$

where $j, k \in [0, 1]$. Next we interpolate along the y-axis,

$$c_i = c_{0,i}(1 - y_d) + c_{1,i}y_d. \tag{3.11}$$

We then interpolate along the z-axis,

$$c = c_0(1 - z_d) + c_1 z_d, \tag{3.12}$$

where c is the approximate function value at the target coordinate.
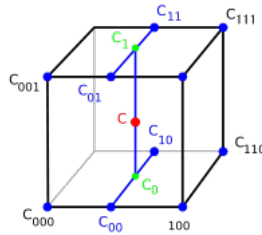
Figure 3.1: Depiction of three-dimensional linear interpolation [12].

3.3 Extrapolation

Since the spectral grids introduced by LORENE can extend to spatial infinity, they typically include collocation points located quite far from the

coordinate origin, well beyond the extent of the rectangular grid used by the `EinsteinToolkit`, to perform the original numerical simulation. Thus, we require a method to take data from the finite-volume Cartesian grid and extrapolate it to arbitrary distances. In doing so, we can take advantage of the fact that all general relativistic field quantities under consideration have known power law fall-off behavior proprtional with distance. Below, we describe our method for fields that exhibit a $1/r$ fall-off behavior, with obvious generalizations for other power law indices.

For target coordinates falling outside the rectangular grid of original numerical simulation data, V, which we assume is centered at the origin, we calculate the ratios

$$x_{\text{ratio}} = \left| \frac{x}{\partial V_x} \right|, \tag{3.13}$$

$$y_{\text{ratio}} = \left| \frac{y}{\partial v_y} \right|, \tag{3.14}$$

$$z_{\text{ratio}} = \left| \frac{z}{\partial V_z} \right|, \tag{3.15}$$

where ∂V is the boundary of V and ∂V_x, ∂V_x, and ∂V_x are the boundaries of V in each axis.

We map a new set of target coordinates, (x', y', z'), onto ∂V along the line segment connecting the points $(0,0,0)$ and (x_0, y_0, z_0) defined by

$$x = x_0 \zeta, \tag{3.16}$$
$$y = y_0 \zeta, \tag{3.17}$$
$$z = z_0 \zeta, \tag{3.18}$$

where $\zeta \in [0, 1]$.

Solving the line equations for the point (x', y', z') we let $\zeta = \frac{1}{\alpha}$, so we have

$$x' = \frac{x_0}{\alpha}, \tag{3.19}$$

$$y' = \frac{y_0}{\alpha}, \tag{3.20}$$

$$z' = \frac{z_0}{\alpha}, \tag{3.21}$$

where $\alpha = \max\{x_{\text{ratio}}, y_{\text{ratio}}, z_{\text{ratio}}\}$.

We interpolate the new target coordinate, (x', y', z'), in the same manner as given in Section 3.2. We then scale the resultant approximation, c', to obtain the approximated function value at the original target coordinate

$$c = \frac{c'}{\alpha},$$
(3.22)

where c is the approximate function value at the target coordinate.

This scaling gives us the desired metric behaviour

$$\lim_{\alpha \to \infty} c = 0.$$
(3.23)

Chapter 4

Field Splitting

It is possible to generate a valid spacetime solution for multiple black holes using superposition for their respective extrinsic curvatures, given the linear nature of the momentum constraint. One may then solve for the conformal factor numerically. Given this breakdown, it is natural to view every field quantity, including the metric components, as representing superpositions of terms taking their source as each of the two black holes, respectively. In this picture, we can decompose every metric quantity into the form $F = f_{bkgrd} + f_1 + f_2$, where f_{bkgrd} describes the asymptotic behavior of the field, and f_1 and f_2 describe the local structure of spacetime around each black hole. Splitting the black hole metrics into two spherical domains allows us to utilize spectral methods on the system when reconstruction of the metrics is desired, but this requires us to choose how we will determine the respective values of f_1 and f_2 at a given point. To achieve this, we have to pick an appropriate function, which we call the splitting function, to scale the metric values at each collocation point such that it that minimizes the error of the reconstructed metrics. The function has to account for the mass of, and distance from, each sigularity, thus adjusting the weight given to each point on the multi-domain grids.

The splitting function candidates we investigate are

$$g(R_{i,j}) = \frac{(M_{i,j}R_{i,j})^n}{(M_{i,j}R_{i,j})^n + \left(\frac{1}{M_{i,j}R_{i,j}}\right)^n} \tag{4.1}$$

for $n \in \{1, 2, 4\}$, where the mass ratio between the pair of black holes of mass

m_i and m_j is

$$M_{i,j} = \frac{m_i}{m_j} \tag{4.2}$$

and the ratio of distances from the point in the multi-domain grid to each singularity is

$$R_{i,j} = \frac{r_j}{r_i}. \tag{4.3}$$

The candidate function must have some particular properties to establish an accurate metric split. First, to ensure each singularity contributes one-hundred percent of the system's metric at its origin, $F = f_i$ with $f_j = 0$ for $i \neq j$, we have

$$g(R) \to 1 \text{ as } R \to \infty \tag{4.4}$$

and

$$g(R) \to 0 \text{ as } R \to 0. \tag{4.5}$$

This means that we will limit our binary pairs to singularities where $g(0) = 1$ for both singularities. Second, since we are using an infinte compactified external domain in order to represent all of space, we must have that

$$g(R) \to \frac{1}{2} \text{ as } R \to 1 \tag{4.6}$$

in order to achieve an equal split at the limits of the domain.

This leaves us with the following local values of the metric components:

$$f_1 = g(R_{1,2}) \cdot (F - f_{\text{bkgrd}}) \tag{4.7}$$

and

$$f_2 = g(R_{2,1}) \cdot (F - f_{\text{bkgrd}}) \tag{4.8}$$

In each case, the coupled metric will be split by the candidate function, and the error measured and analyzed.

$$G(R_{1,2}) = \frac{R_{1,2}}{R_{1,2}+1/R_{1,2}}$$
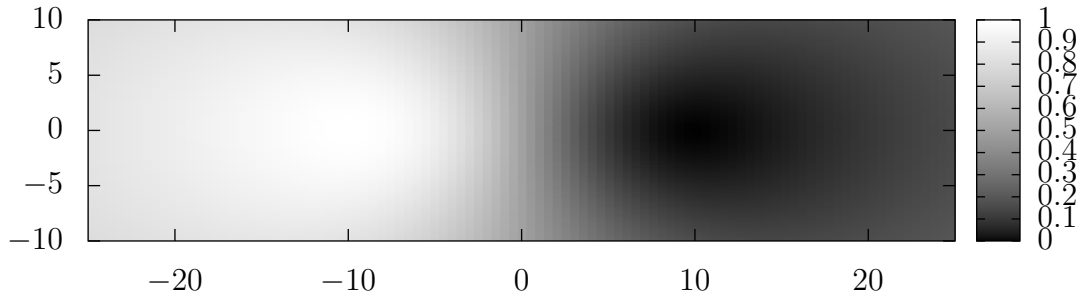
$$G(R_{1,2}) = \frac{R_{1,2}^2}{R_{1,2}^2+1/R_{1,2}^2}$$
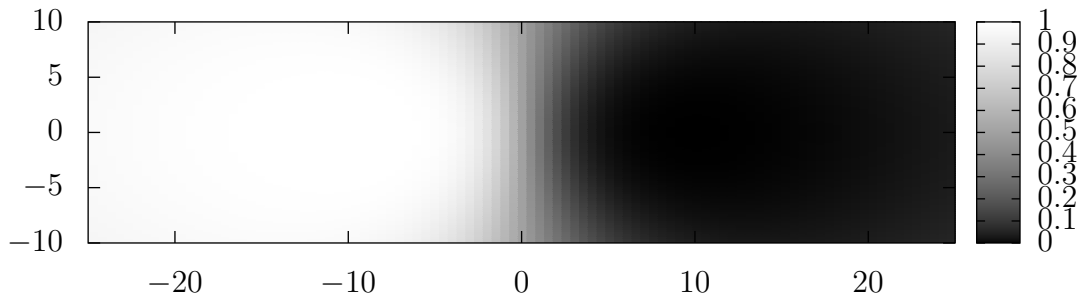
$$g(R_{1,2}) = \frac{R_{1,2}^4}{R_{1,2}^4+1/R_{1,2}^4}$$
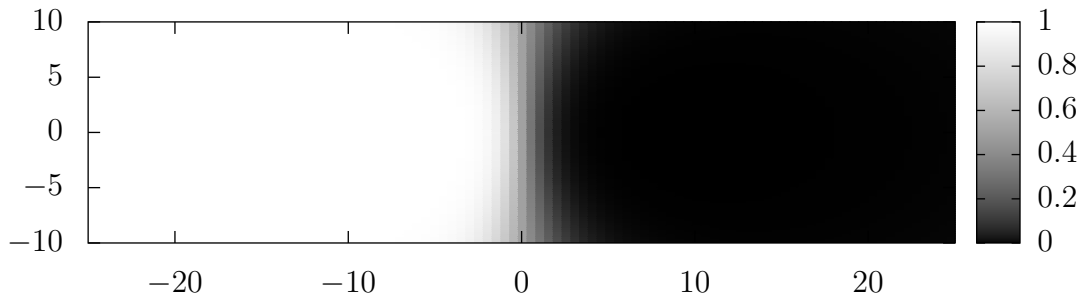
Figure 4.1: Heat maps of three candidate splitting functions used for a singularity located at $(-10, 0, 0)$ with its binary partner located at $(10, 0, 0)$ in $\mathbb{R}^3$.

Chapter 5

Multi-Domain Spectral Method

The goal of utilizing a multi-domain spectral scheme is to expand each domain as a finite sum. Any singular function can be represented in terms of a Taylor series by

$$f(x, y, z) = \sum_{i,j,k} c_{i,j,k} x_i y_j z_k. \tag{5.1}$$

By the usual coordinate transformation we have

$$f(r, \theta, \phi) = \sum_{m=-M}^{M} \sum_{\ell=|m|}^{L} r^\ell T(r^2) \sin^{|m|} \theta P_{\ell-|m|}(\cos \theta) e^{im\phi}, \tag{5.2}$$

where L and M are positive integers, $L > M$, $P_{\ell-|m|}$ is some polynomial of degree $\ell - |m|$ and $T(r^2)$ is some even polynomial.

The spectral expansion will be with repect to (ξ, θ, ϕ) instead of the physical coordinates (r, θ, ϕ). The basis functions are chosen such that they may be put in the form $X(\xi)\Theta(\theta)\Phi(\phi)$.

5.1 ϕ Expansion

Since ϕ is periodic, the Fourier series is chosen as the basis functions

$$\Phi_k(\phi) = e^{ik\phi}, \qquad \frac{-N_\phi}{2} \leq k \leq \frac{N_\phi}{2}, \tag{5.3}$$

where N_ϕ is the number of degrees of freedom in ϕ [5]. The collocation points are defined as

$$\phi_k = \frac{2\pi k}{N_\phi}, \qquad k = 0, \ldots, N_\phi - 1 \tag{5.4}$$

16

and are equally spaced in $[0, 2\pi)$[6]. So we have the approximation formula for the ϕ expansion

$$I_{N_\phi} f_\phi(\phi) = \sum_{k=-N_\phi/2}^{N_\phi/2} a_k \Phi_k(\phi), \qquad (5.5)$$

where

$$a_k = \frac{1}{N_\phi} \sum_{k=0}^{N_\phi-1} f_\phi(\phi_k) e^{-ik\phi_k} \qquad (5.6)$$

are the discrete Fourier coefficients [6].

5.2 θ Expansion

In θ we take the basis functions as

$$\Theta_{kj}(\theta) = \begin{cases} \cos(j\theta), & 0 \le j \le N_\theta - 1 \text{ for } m \text{ even} \\ \sin(j\theta), & 0 \le j \le N_\theta - 1 \text{ for } m \text{ odd} \end{cases}, \qquad (5.7)$$

where N_θ is the number of degrees of freedom in θ [5]. The collocation points are defined as

$$\theta_j = \frac{\pi j}{N_\theta - 1}, \qquad j = 0, \ldots, N_\theta - 1 \qquad (5.8)$$

and are equally spaced in $[0, \pi]$ [6]. So we have the approximation formula for the θ expansion

$$I_{N_\theta} f_\theta(\theta) = \sum_{j=0}^{N_\theta-1} a_j \Theta_j(\theta), \qquad (5.9)$$

where

$$a_0 = \frac{1}{N_\theta} f_\theta(\theta_0) \qquad (5.10)$$

and

$$a_j = \frac{2}{N_\theta} \sum_{j=1}^{N_\theta-1} f_\theta(\theta_j) e^{-ij\theta_j} \qquad (5.11)$$

are the even Fourier coefficients [6].

5.3 ξ Expansion

For the nucleus of the multi-domain grids we use the basis functions

$$X_{kji} = \begin{cases} T_{2i}(\xi), & 0 \le i \le N_r - 1 \text{ for } j \text{ even} \\ T_{2i+1}(\xi), & 0 \le i \le N_r - 2 \text{ for } j \text{ odd} \end{cases}, \tag{5.12}$$

where N_r is the number of degrees of freedom in r, and T_n is the nth degree Chebyshev polynomial [5]. The collocation points are defined as

$$\xi_i = \sin\left(\frac{\pi}{2} \frac{i}{N_r - 1}\right), \quad i = 0, \dots, N_r - 1 \tag{5.13}$$

and are spaced to minimize the Runge phenomenon [6]. For the intermediate and external domains we use

$$X_{kji} = T_i(\xi) \tag{5.14}$$

as basis functions, and the collocation points

$$\xi_i = -\cos\left(\frac{\pi i}{N_r - 1}\right), \quad i = 0, \dots, N_r - 1. \tag{5.15}$$

This leaves us with the radial approximation formula

$$I_{N_r} f_r(\xi) = \sum_{i=0}^{N_r-1} a_i X_{kji}(\xi), \tag{5.16}$$

where

$$a_0 = \frac{1}{N_r} f_r(\xi_0) T_0(\xi_0) \tag{5.17}$$

and

$$a_i = \frac{2}{N_r} \sum_{i=1}^{N_r-1} f_r(\xi_i) T_i(\xi_i) \tag{5.18}$$

are the even Chebyshev coefficients [6].
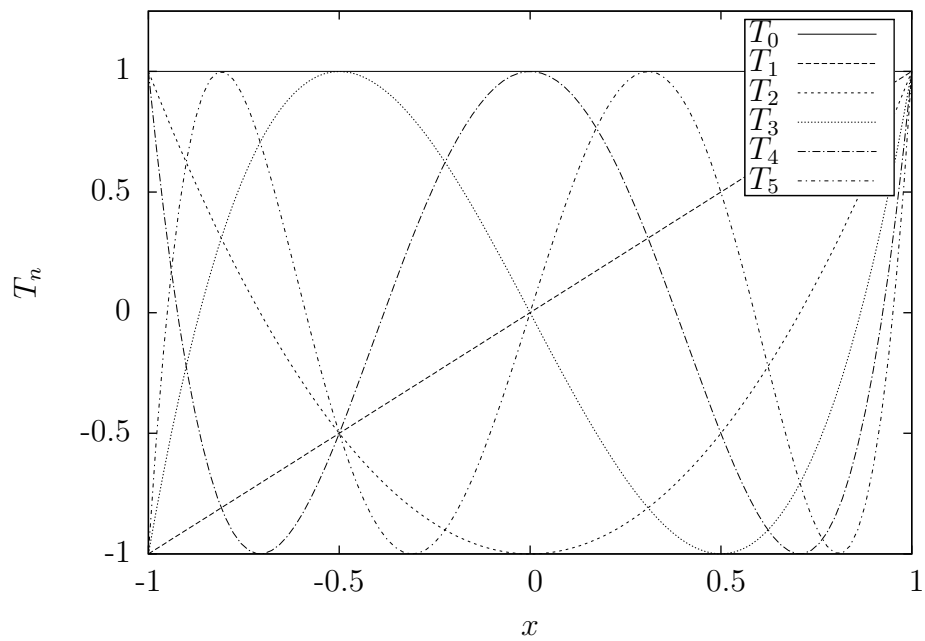
Figure 5.1: Examples of Chebyshev polynomials.

Chapter 6

Numerical Error

Error is introduced in two places using this method. The first is when data is interpolated onto the LORENE grids via cubic and linear interpolating routines, and the second is when the field is reconstructed using spectral expansions. The reconstruction error consists of error from the difference between the exact function and the interpolant, as well as truncation error caused by cutting off higher order modes of the series expansion. We look at the error introduced and verify that it follows expected fall-offs based on grid size and interpolation technique.

We compare the error introduced when data is approximated at the collocation points over multiple Cartesian grid sizes. The error calculated is the root-mean-square deviation (RMSD) and represents the difference between approximated values and exact values.

$$RMSD = \sqrt{\frac{\sum_{k=1}^{n}(\hat{x} - x)^2}{n}}, \tag{6.1}$$

where $\hat{x}$ is the approximated value, x is the exact value, and n is the sample size.

To test the error introduced, we use the function

$$f(r, \theta, \phi) = \left(\frac{r^2}{\sqrt{1 + r^6}}\right) \cos(\theta) \sin(\theta)[\sin(\phi) + \cos(\phi)] \tag{6.2}$$

which is exactly representable by the spectral expansion methods used.

6.1   Single-Domain Error

We begin by generating Cartesian grids of varying densities to investigate the expected interpolation error introduced as data is transferred from the Cartesian grid to the multi-domain grids generated from the LORENE routines. Next, we feed the exact values of Equation (6.2) into the collocation points of the multi-domain grid and compare it to the spectral expansion generated by the LORENE routines at the same points, looking for minimal error, which signifies that the expansion routines work as designed. Finally, we combine both interpolation and spectral expansion and look at the error produced when a Cartesian grid of data generated from Equation (6.2) is interpolated onto a multi-domain grid, spectrally expanded, and then calculated at the original Cartesian grid points to determine the error of a fully reconstructed field. In all cases, the RMSD is then calculated in the standard way using Equation (6.1).

6.1.1   Interpolation Error

Interpolating data onto the LORENE grid will introduce error. We aim to quantify how much is introduced using different Cartesian grid densities. We utilize two interpolation routines: linear and cubic. We expect the linear routine to produce error fall-off approximately $\propto h^2$, and the cubic routine to produce error fall-off approximately $\propto h^4$.

Figures 6.1 and 6.2 show the interpolation error, ε_I, as a function of Cartesian grid point spacing, h, associated with linear and cubic interpolation routines, respectively. We see that the error approximately follows a power law convergence $\varepsilon_I \propto h^{-\beta}$, as seen by the tracking curve plotted in each figure, as expected. The Cartesian grids are in the interval $[-10, 10]$ and have a varying grid spacing of $h = 2.22222$ to $h = 2 \times 10^{-8}$. Note that only the points in each grid needed for the interpolation are loaded into memory, thus reducing the computational overhead. The multi-domain grid extends to spacial infinity due to the exterior domain compactification. The x-axis is the rectangular grid spacing h, and the y-axis is the interpolation error ε_I. Both the linear and cubic interpolation error is calculated using only the points contained within the interior voxels of the Cartesian grid. Points contained in any of the outermost voxels where only the linear interpolation routine can function, as well as any points exterior to the Cartesian grid where only extrapolation takes place, were excluded so that the resulting error from each

routine may be compared properly over the same domain. From the graph we can see both the linear and cubic interpolation routines exhibit power law fall-off, as expected. We see that saturation begins to occur at approximately $h = 1 \times 10^{-8}$ in the linear case and occurs at approximately $h = 1 \times 10^{-4}$ in the cubic case.
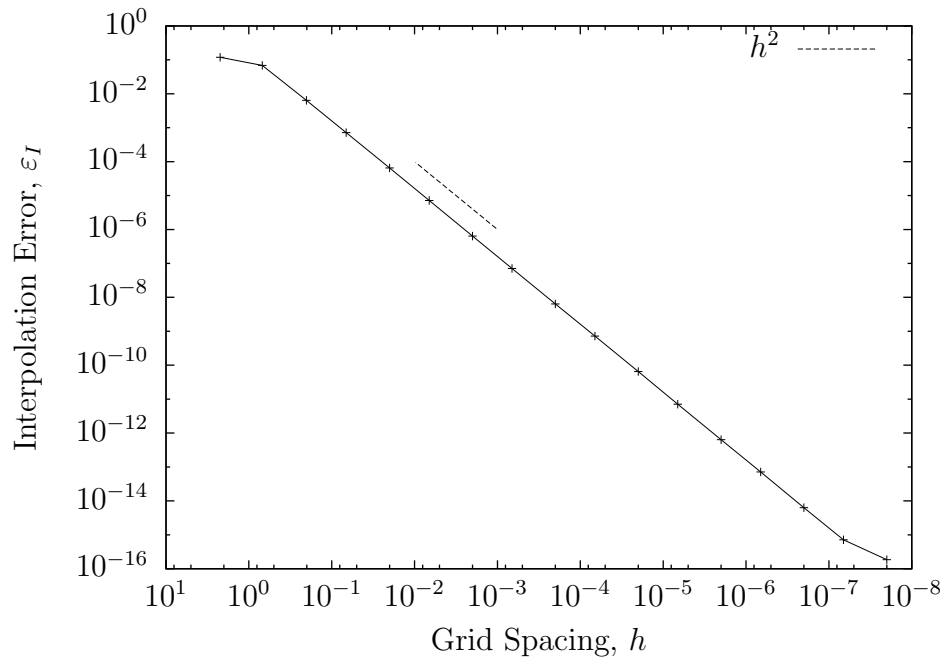
Figure 6.1: The interpolation error, ε_I, of a linear interpolating routine as a function of grid spacing, h, over the interval $[-10, 10]$ on all axes. The multi-domain grid interpolated onto consists of three domains: an inner domain, an intermediate domain, and a compactified external domain that extends to spacial infinity.
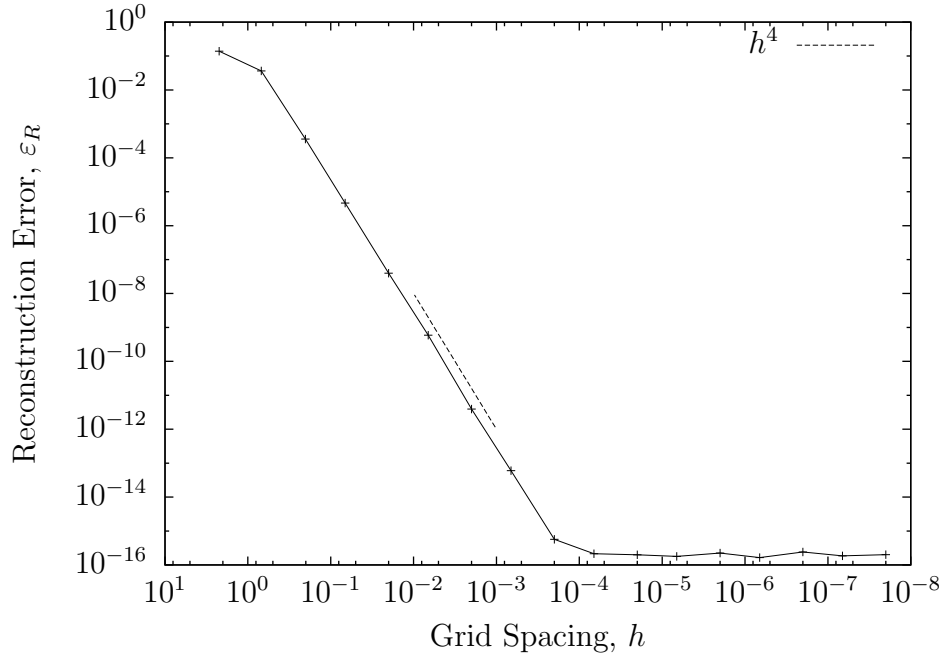
Figure 6.2: The interpolation error, ε_I, of a cubic interpolating routine as a function of grid spacing, h, over the interval $[-10, 10]$ on all axes. The multi-domain grid interpolated onto consists of three domains: an inner domain, an intermediate domain, and a compactified external domain that extends to spacial infinity.

6.1.2   Reconstruction Error

When reconstructing the field with a spectral expansion, we expect error to be introduced into the data. The error is the result of a difference in the exact function and that function's interpolant, as well as truncation error caused by cutting off higher order modes of the series expansion. We expect the error will become evanescent when a large number of collocation points is used in the multi-domain grid. We verify an exactly representable function in (r, θ, ϕ) inputted onto the LORENE spectral expansion routine can be extracted as an approximated function with negligible error introduced, confirming the spectral routines work as expected.

As we can see from the results in Figure 6.3, reconstruction error, ε_R, becomes evanescent as the number of collocation points increases when the

routine is provided an exactly representable function. Saturation occurs at approximately 3.5×10^5 collocation points. After the saturation point, further refinement of the multi-domain grid will not yield better accuracy and will only add to the computational overhead of the routine.
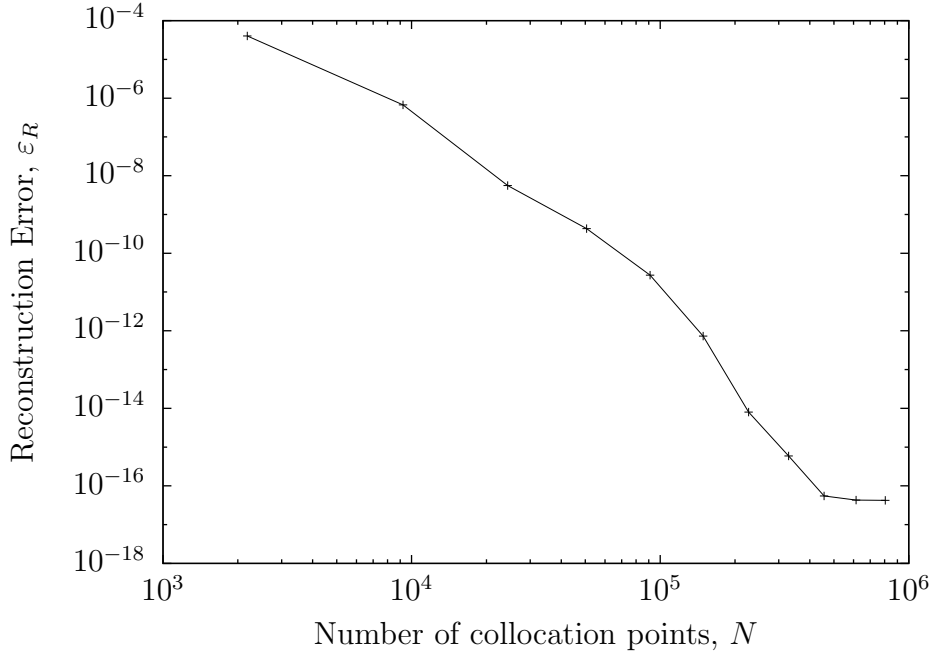
Figure 6.3: The reconstruction error, ε_R, of the spectral expansion over an exactly representable function, as a function of the number of collocation points, N, in the multi-domain grid. The multi-domain grid used for the spectral expansion consists of four domains: an inner domain, two intermediate domains, and a compactified external domain that extends to spacial infinity.

6.1.3 Reconstruction Error of an Interpolated Data Set

In this section we look at the combined effects of interpolation and reconstruction error. To measure this error we interpolate Cartesian grids comprised of equally spaced points, whose values were once again computed from Equation (6.2), onto multi-domain grids containing varying numbers of collocation points. We then extract the spectral expansion approximation functions

from the LORENE routines and approximate the values of the metric at the coordinates in the Cartesian grids in order to compare the original values to the spectrally expanded values. Due to the high number of points needed to calculate the error, we use a reduced sample set.

Figure 6.4 shows the total error, ε, as a function of Cartesian grid-point spacing, h, associated with the linear and cubic interpolation routines, respectively. We see that saturation occurs at a much higher error value due to under resolution by the spectral expansion in the data series with fewer degrees of freedom.
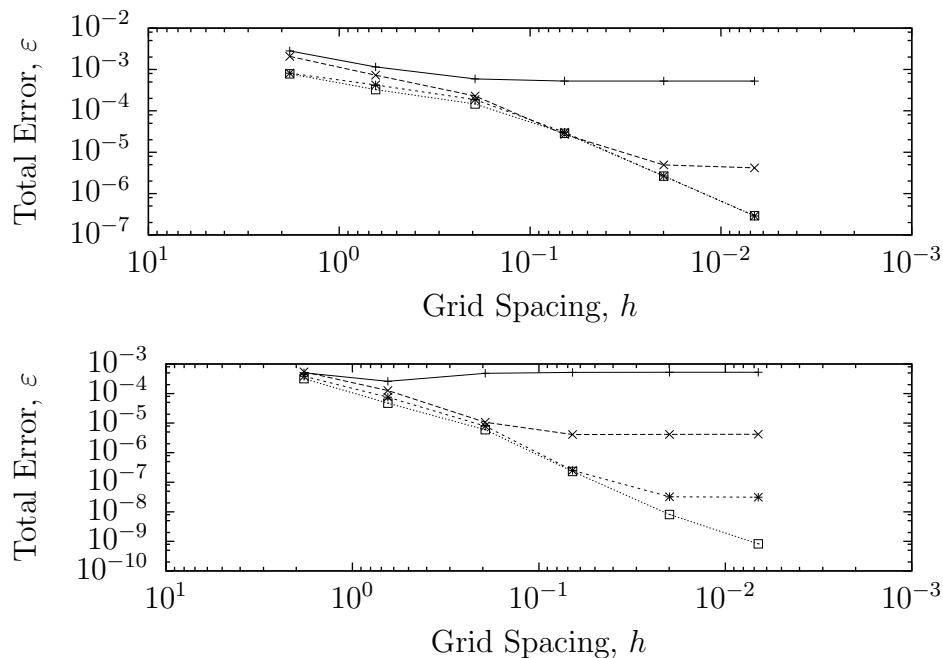
Figure 6.4: The total error, ε, introduced during the interpolation and subsequent spectral expansion as a function of grid-point spacing, h, over the interval $[-10, 10]$ in $\mathbb{R}^3$. The multi-domain grid interpolated onto and then spectrally expanded consists of three domains: an inner domain, one intermediate domain, and a compactified external domain that extends to spacial infinity. The first data series $(+)$ shows the error associated with a multi-domain grid consisting of $1,638$ collocation points. The second data series $(\times)$ shows the error associated with a multi-domain grid consisting of $37,962$ collocation points. The third data series $(*)$ shows the error associated with a multi-domain grid consisting of $170,190$ collocation points. The fourth data series $(\square)$ shows the error associated with a multi-domain grid consisting of $460,530$ collocation points. The upper plot utilized a linear interpolation routine and the lower plot utilized a cubic interpolation routine.

Figure 6.5 shows the total error, ε, as a function of the number of collocation points in the multi-domain grid, N, associated with the linear and cubic interpolation routines, respectively. In this case, saturation at higher error is driven by initial data grid density.
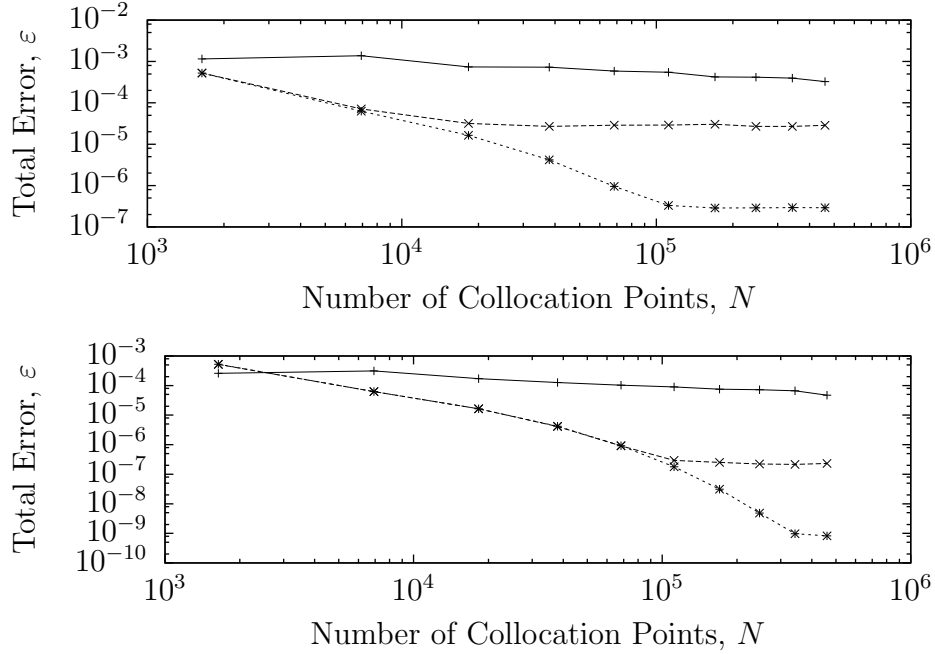
Figure 6.5: The total error, ε, introduced during the interpolation and subsequent spectral expansion as a function of the number of collocation points, N, over the interval $[-10, 10]$ in $\mathbb{R}^3$. The multi-domain grid interpolated onto and then spectrally expanded consists of three domains: an inner domain, one intermediate domain, and a compactified external domain that extends to spacial infinity. The first data series $(+)$ shows the error associated with a Cartesian grid spacing $h = 0.645161$. The second data series $(\times)$ shows the error associated with a Cartesian grid spacing $h = 0.0660066$. The third data series $(*)$ shows the error associated with a Cartesian grid spacing $h = 0.00666001$. The upper plot utilized a linear interpolation routine and the lower plot utilized a cubic interpolation routine.

6.2 Two-Domain Error

With the linear and cubic interpolation error behaving as expected and the spectral expansion error becoming evanescent as one would expect, we turn our attention to the behavior of the these errors when implemented in a two domain scheme, with the addition of black hole spacetime metric decoupling. Splitting the fields of the black holes in an optimal manner minimizes the

error of the spectral expansion.

Figure 6.6 shows the total error, ε, from each of the candidate splitting functions, defined in Section 4, as a function of the number of collocation points, N, used in the calculation. The original field was given by Equation (6.2) over the domain $[-128, 128]$ in $\mathbb{R}^3$ with the black holes centered at $(\pm 10, 0, 0)$. We see each splitting function resulting in approximately equal error.
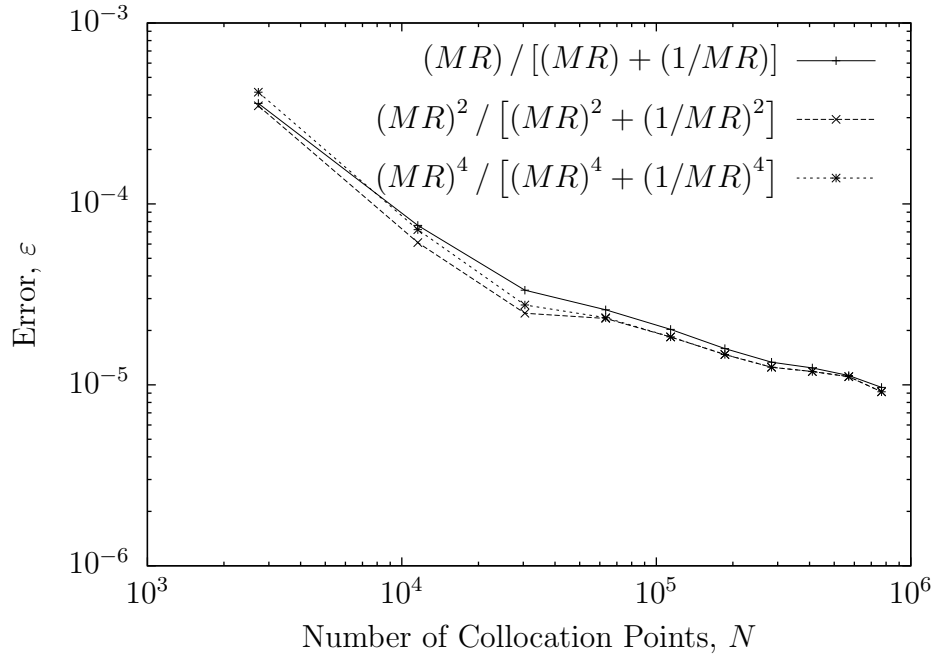
Figure 6.6: Results of testing to compare the candidate metric splitting functions effect on accuracy of the spectral expansion of a binary black hole system. The total error, ε, of the interpolation and subsequent reconstruction of the original field as a function of the number of collocation points, N, over the interval $[-128, 128]$ in $\mathbb{R}^3$. Each multi-domain grid interpolated onto and then spectrally expanded consists of five domains: an inner domain, three intermediate domains, and a compactified external domain that extends to spacial infinity. A data set is plotted for each splitting function given by Equation (4.1) for $n \in \{1, 2, 4\}$.

Chapter 7

Results

Our goal was to minimize the storage requirements of general relativistic evolution simulations and, at the same time, minimize the error introduced by the compression routine. In order to do this we needed to consider both the initial Cartesian grid density used for the interpolation, and the multi-domain grid density used for the spectral expansion.

In terms of the optimal grid density for our interpolation routines, we are looking for a Cartesian grid density that achieves maximum accuracy. For the cubic interpolation routine, this occurs below the grid spacing $h = 1 \times 10^{-4}$, keeping in mind that the outer voxels utilize a linear interpolation routine, and saturation occurs below $h = 1 \times 10^{-8}$ in this case. If the outer voxels contain relatively smooth data then the saturation density of the cubic routine should suffice, otherwise the linear saturation density should be considered, although the computational overhead will be greater.

To reconstruct the metrics with suitable accuracy, the spectral expansion should utilize grid densities that, like in the case of the optimal interpolation grid densities, minimize error and computational requirements. This occurs at approximately 3.5×10^5 collocation points in our test cases. Some variabililty can occur here due to the number of domains used in the reconstruction and the interval of each domain. Optimally, the highest density of collocation points will occur where the data is most dynamic (e.g. in the immediate area of the singularity, near an accretion disk, etc...).

In order to optimize accuracy, we tested multiple functions to decouple the black holes' metric fields. The different functions assigned differing amounts of the combined metric F to each isolated metric f_1 and f_2.

In Figure 6.6 we see that each splitting function tested yields approximately

equal error. No one function stands out as more accurate, though at higher collocation point counts, greater than approximately 10^5 points per grid, the three functions error converges to the same value. From a computational perspective, choosing the function

$$g(R_{i,j}) = \frac{(M_{i,j}R_{i,j})}{(M_{i,j}R_{i,j}) + \left(\frac{1}{M_{i,j}R_{i,j}}\right)} \tag{7.1}$$

will lower the computational overhead required since fewer exponents are used, though the savings would be negligible.

Figure 7.1 shows the relative compressed file sizes for the three splitting functions defined in Section 4 over varying multi-domain grid densities. No appreciable difference in file storage size can be distinguished between different splitting functions, which is to be expected since the storage requirements are a function of total data points, not the value of the data itself.

Now, when comparing the compressed data to the original data in terms of storage space, we have a significant reduction in storage requirements. Table 7.1 summarizes the data compression achieved by our routines. This level of compression allows an immense amount of data storage. A metric field could be stored for future work and, due to the nature of the spectral expansion, can be reconstructed in any desired configuration. It is not necessary to reconstruct the original field, as the expansion can accept any arbitrary coordinate (r, θ, ϕ). In addition, the use of multiple domains allows this method to be utilized in not only black hole calculations, where the field is smooth everywhere but at the singularity, but also in calculations involving objects where the surface is non-differentiable. By aligning the boundary surface, $\mathcal{S}_0$, of the nucleus, D_0, we avoid the issues associated with non-differentiability.
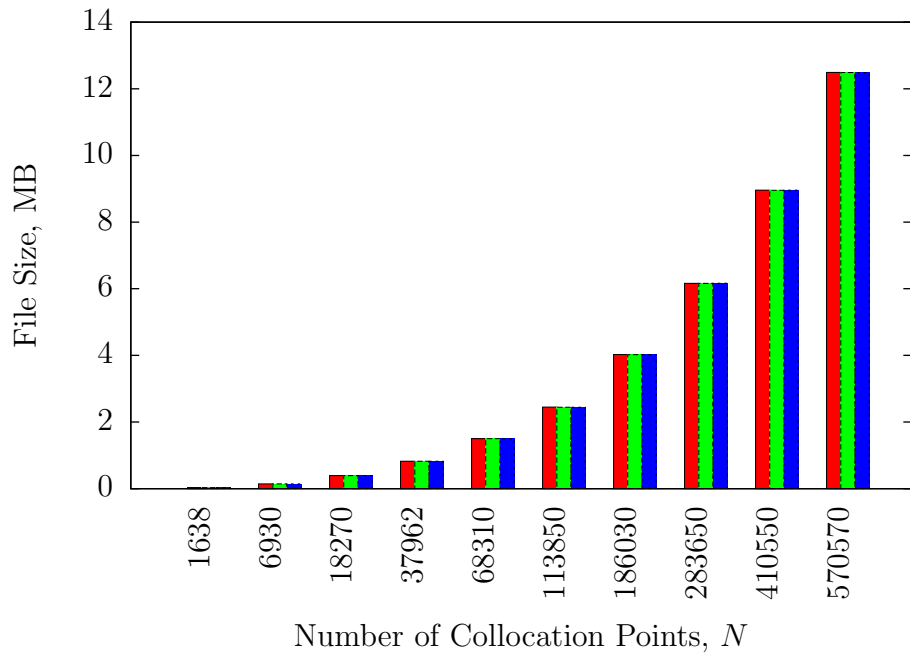
Figure 7.1: Histogram of compressed file sizes (MB) for the three splitting functions tested as a function of the number of collocation points, N, in each multi-domain grid. Each set of collocation points is associated with Equation (4.1) where the left column is calculated with $n = 1$, the center column is calculated with $n = 2$, and the right column is calculated with $n = 4$.

Collocation Points	Size (MB)	Original Size (MB)	% Reduction	Error
2730	0.052680		99.99%	0.000359739
11550	0.235448		99.96%	7.61397e-05
30450	0.638737		99.89%	3.33353e-05
63270	1.345334		99.76%	2.59806e-05
113850	2.447111	568.6	99.57%	2.0246e-05
186030	4.023237		99.29%	1.58614e-05
283650	6.163660		98.92%	1.33373e-05
410550	8.959538		98.42%	1.24144e-05
570570	12.491530		97.80%	1.12602e-05
767550	16.847986		97.04%	9.67996e-06

Table 7.1: Summary of data compression achieved through multi-domain spectral methods. The initial grid size consists of 201 points over the interval $[-128, 128]$ in $\mathbb{R}^3$.

References

[1] B. P. Abbott, R. Abbott, T. D. Abbott, M. R. Abernathy, F. Acernese, K. Ackley, C. Adams, T. Adams, P. Addesso, R. X. Adhikari, V. B. Adya, C. Affeldt, M. Agathos, K. Agatsuma, N. Aggarwal, O. D. Aguiar, L. Aiello, A. Ain, P. Ajith, B. Allen, A. Allocca, P. A. Altin, S. B. Anderson, W. G. Anderson, K. Arai, M. A. Arain, M. C. Araya, C. C. Arceneaux, J. S. Areeda, N. Arnaud, K. G. Arun, S. Ascenzi, G. Ashton, M. Ast, S. M. Aston, P. Astone, P. Aufmuth, C. Aulbert, S. Babak, P. Bacon, M. K. M. Bader, P. T. Baker, F. Baldaccini, G. Ballardin, S. W. Ballmer, J. C. Barayoga, S. E. Barclay, B. C. Barish, D. Barker, F. Barone, B. Barr, L. Barsotti, M. Barsuglia, D. Barta, J. Bartlett, M. A. Barton, I. Bartos, R. Bassiri, A. Basti, J. C. Batch, C. Baune, V. Bavigadda, M. Bazzan, B. Behnke, M. Bejger, C. Belczynski, A. S. Bell, C. J. Bell, B. K. Berger, J. Bergman, G. Bergmann, C. P. L. Berry, D. Bersanetti, A. Bertolini, J. Betzwieser, S. Bhagwat, R. Bhandare, I. A. Bilenko, G. Billingsley, J. Birch, R. Birney, O. Birnholtz, S. Biscans, A. Bisht, M. Bitossi, C. Biwer, M. A. Bizouard, J. K. Blackburn, C. D. Blair, D. G. Blair, R. M. Blair, S. Bloemen, O. Bock, T. P. Bodiya, M. Boer, G. Bogaert, C. Bogan, A. Bohe, P. Bojtos, C. Bond, F. Bondu, R. Bonnand, B. A. Boom, R. Bork, V. Boschi, S. Bose, Y. Bouffanais, A. Bozzi, C. Bradaschia, P. R. Brady, V. B. Braginsky, M. Branchesi, J. E. Brau, T. Briant, A. Brillet, M. Brinkmann, V. Brisson, P. Brockill, A. F. Brooks, D. A. Brown, D. D. Brown, N. M. Brown, C. C. Buchanan, A. Buikema, T. Bulik, H. J. Bulten, A. Buonanno, D. Buskulic, C. Buy, R. L. Byer, M. Cabero, L. Cadonati, G. Cagnoli, C. Cahillane, J. C. Bustillo, T. Callister, E. Calloni, J. B. Camp, K. C. Cannon, J. Cao, C. D. Capano, E. Capocasa, F. Carbognani, S. Caride, J. C. Diaz, C. Casentini, S. Caudill, M. Cavaglià, F. Cavalier, R. Cavalieri, G. Cella, C. B. Cepeda, L. C. Baiardi, G. Cerretani, E. Cesarini, R. Chakraborty,

T. Chalermsongsak, S. J. Chamberlin, M. Chan, S. Chao, P. Charlton, E. Chassande-Mottin, H. Y. Chen, Y. Chen, C. Cheng, A. Chincarini, A. Chiummo, H. S. Cho, M. Cho, J. H. Chow, N. Christensen, Q. Chu, S. Chua, S. Chung, G. Ciani, F. Clara, J. A. Clark, F. Cleva, E. Coccia, P.-F. Cohadon, A. Colla, C. G. Collette, L. Cominsky, M. Constancio, A. Conte, L. Conti, D. Cook, T. R. Corbitt, N. Cornish, A. Corsi, S. Cortese, C. A. Costa, M. W. Coughlin, S. B. Coughlin, J.-P. Coulon, S. T. Countryman, P. Couvares, E. E. Cowan, D. M. Coward, M. J. Cowart, D. C. Coyne, R. Coyne, K. Craig, J. D. E. Creighton, T. D. Creighton, J. Cripe, S. G. Crowder, A. M. Cruise, A. Cumming, L. Cunningham, E. Cuoco, T. D. Canton, S. L. Danilishin, S. D'Antonio, K. Danzmann, N. S. Darman, C. F. Da Silva Costa, V. Dattilo, I. Dave, H. P. Daveloza, M. Davier, G. S. Davies, E. J. Daw, R. Day, S. De, D. DeBra, G. Debreczeni, J. Degallaix, M. De Laurentis, S. Deléglise, W. Del Pozzo, T. Denker, T. Dent, H. Dereli, V. Dergachev, R. T. DeRosa, R. De Rosa, R. DeSalvo, S. Dhurandhar, M. C. Díaz, L. Di Fiore, M. Di Giovanni, A. Di Lieto, S. Di Pace, I. Di Palma, A. Di Virgilio, G. Dojcinoski, V. Dolique, F. Donovan, K. L. Dooley, S. Doravari, R. Douglas, T. P. Downes, M. Drago, R. W. P. Drever, J. C. Driggers, Z. Du, M. Ducrot, S. E. Dwyer, T. B. Edo, M. C. Edwards, A. Effler, H.-B. Eggenstein, P. Ehrens, J. Eichholz, S. S. Eikenberry, W. Engels, R. C. Essick, T. Etzel, M. Evans, T. M. Evans, R. Everett, M. Factourovich, V. Fafone, H. Fair, S. Fairhurst, X. Fan, Q. Fang, S. Farinon, B. Farr, W. M. Farr, M. Favata, M. Fays, H. Fehrmann, M. M. Fejer, D. Feldbaum, I. Ferrante, E. C. Ferreira, F. Ferrini, F. Fidecaro, L. S. Finn, I. Fiori, D. Fiorucci, R. P. Fisher, R. Flaminio, M. Fletcher, H. Fong, J.-D. Fournier, S. Franco, S. Frasca, F. Frasconi, M. Frede, Z. Frei, A. Freise, R. Frey, V. Frey, T. T. Fricke, P. Fritschel, V. V. Frolov, P. Fulda, M. Fyffe, H. A. G. Gabbard, J. R. Gair, L. Gammaitoni, S. G. Gaonkar, F. Garufi, A. Gatto, G. Gaur, N. Gehrels, G. Gemme, B. Gendre, E. Genin, A. Gennai, J. George, L. Gergely, V. Germain, A. Ghosh, A. Ghosh, S. Ghosh, J. A. Giaime, K. D. Giardina, A. Giazotto, K. Gill, A. Glaefke, J. R. Gleason, E. Goetz, R. Goetz, L. Gondan, G. González, J. M. G. Castro, A. Gopakumar, N. A. Gordon, M. L. Gorodetsky, S. E. Gossan, M. Gosselin, R. Gouaty, C. Graef, P. B. Graff, M. Granata, A. Grant, S. Gras, C. Gray, G. Greco, A. C. Green, R. J. S. Greenhalgh, P. Groot, H. Grote, S. Grunewald, G. M. Guidi, X. Guo, A. Gupta, M. K. Gupta, K. E. Gushwa, E. K. Gustafson, R. Gustafson, J. J. Hacker, B. R. Hall, E. D. Hall, G. Ham-

mond, M. Haney, M. M. Hanke, J. Hanks, C. Hanna, M. D. Hannam,
J. Hanson, T. Hardwick, J. Harms, G. M. Harry, I. W. Harry, M. J.
Hart, M. T. Hartman, C.-J. Haster, K. Haughian, J. Healy, J. Heefner,
A. Heidmann, M. C. Heintze, G. Heinzel, H. Heitmann, P. Hello, G. Hem-
ming, M. Hendry, I. S. Heng, J. Hennig, A. W. Heptonstall, M. Heurs,
S. Hild, D. Hoak, K. A. Hodge, D. Hofman, S. E. Hollitt, K. Holt, D. E.
Holz, P. Hopkins, D. J. Hosken, J. Hough, E. A. Houston, E. J. Howell,
Y. M. Hu, S. Huang, E. A. Huerta, D. Huet, B. Hughey, S. Husa, S. H.
Huttner, T. Huynh-Dinh, A. Idrisy, N. Indik, D. R. Ingram, R. Inta,
H. N. Isa, J.-M. Isac, M. Isi, G. Islas, T. Isogai, B. R. Iyer, K. Izumi,
M. B. Jacobson, T. Jacqmin, H. Jang, K. Jani, P. Jaranowski, S. Jawahar,
F. Jiménez-Forteza, W. W. Johnson, N. K. Johnson-McDaniel, D. I. Jones,
R. Jones, R. J. G. Jonker, L. Ju, K. Haris, C. V. Kalaghatgi, V. Kalogera,
S. Kandhasamy, G. Kang, J. B. Kanner, S. Karki, M. Kasprzack, E. Kat-
savounidis, W. Katzman, S. Kaufer, T. Kaur, K. Kawabe, F. Kawazoe,
F. Kéfélian, M. S. Kehl, D. Keitel, D. B. Kelley, W. Kells, R. Kennedy,
D. G. Keppel, J. S. Key, A. Khalaidovski, F. Y. Khalili, I. Khan, S. Khan,
Z. Khan, E. A. Khazanov, N. Kijbunchoo, C. Kim, J. Kim, K. Kim,
N.-G. Kim, N. Kim, Y.-M. Kim, E. J. King, P. J. King, D. L. Kinzel, J. S.
Kissel, L. Kleybolte, S. Klimenko, S. M. Koehlenbeck, K. Kokeyama,
S. Koley, V. Kondrashov, A. Kontos, S. Koranda, M. Korobko, W. Z.
Korth, I. Kowalska, D. B. Kozak, V. Kringel, B. Krishnan, A. Królak,
C. Krueger, G. Kuehn, P. Kumar, R. Kumar, L. Kuo, A. Kutynia,
P. Kwee, B. D. Lackey, M. Landry, J. Lange, B. Lantz, P. D. Lasky,
A. Lazzarini, C. Lazzaro, P. Leaci, S. Leavey, E. O. Lebigot, C. H. Lee,
H. K. Lee, H. M. Lee, K. Lee, A. Lenon, M. Leonardi, J. R. Leong,
N. Leroy, N. Letendre, Y. Levin, B. M. Levine, T. G. F. Li, A. Libson,
T. B. Littenberg, N. A. Lockerbie, J. Logue, A. L. Lombardi, L. T.
London, J. E. Lord, M. Lorenzini, V. Loriette, M. Lormand, G. Lo-
surdo, J. D. Lough, C. O. Lousto, G. Lovelace, H. Lück, A. P. Lundgren,
J. Luo, R. Lynch, Y. Ma, T. MacDonald, B. Machenschalk, M. MacInnis,
D. M. Macleod, F. Magaña Sandoval, R. M. Magee, M. Mageswaran,
E. Majorana, I. Maksimovic, V. Malvezzi, N. Man, I. Mandel, V. Mandic,
V. Mangano, G. L. Mansell, M. Manske, M. Mantovani, F. Marchesoni,
F. Marion, S. Márka, Z. Márka, A. S. Markosyan, E. Maros, F. Martelli,
L. Martellini, I. W. Martin, R. M. Martin, D. V. Martynov, J. N. Marx,
K. Mason, A. Masserot, T. J. Massinger, M. Masso-Reid, F. Matichard,
L. Matone, N. Mavalvala, N. Mazumder, G. Mazzolo, R. McCarthy, D. E.

McClelland, S. McCormick, S. C. McGuire, G. McIntyre, J. McIver, D. J. McManus, S. T. McWilliams, D. Meacher, G. D. Meadors, J. Meidam, A. Melatos, G. Mendell, D. Mendoza-Gandara, R. A. Mercer, E. Merilh, M. Merzougui, S. Meshkov, C. Messenger, C. Messick, P. M. Meyers, F. Mezzani, H. Miao, C. Michel, H. Middleton, E. E. Mikhailov, L. Milano, J. Miller, M. Millhouse, Y. Minenkov, J. Ming, S. Mirshekari, C. Mishra, S. Mitra, V. P. Mitrofanov, G. Mitselmakher, R. Mittleman, A. Moggi, M. Mohan, S. R. P. Mohapatra, M. Montani, B. C. Moore, C. J. Moore, D. Moraru, G. Moreno, S. R. Morriss, K. Mossavi, B. Mours, C. M. Mow-Lowry, C. L. Mueller, G. Mueller, A. W. Muir, A. Mukherjee, D. Mukherjee, S. Mukherjee, N. Mukund, A. Mullavey, J. Munch, D. J. Murphy, P. G. Murray, A. Mytidis, I. Nardecchia, L. Naticchioni, R. K. Nayak, V. Necula, K. Nedkova, G. Nelemans, M. Neri, A. Neunzert, G. Newton, T. T. Nguyen, A. B. Nielsen, S. Nissanke, A. Nitz, F. Nocera, D. Nolting, M. E. N. Normandin, L. K. Nuttall, J. Oberling, E. Ochsner, J. O'Dell, E. Oelker, G. H. Ogin, J. J. Oh, S. H. Oh, F. Ohme, M. Oliver, P. Oppermann, R. J. Oram, B. O'Reilly, R. O'Shaughnessy, C. D. Ott, D. J. Ottaway, R. S. Ottens, H. Overmier, B. J. Owen, A. Pai, S. A. Pai, J. R. Palamos, O. Palashov, C. Palomba, A. Pal-Singh, H. Pan, Y. Pan, C. Pankow, F. Pannarale, B. C. Pant, F. Paoletti, A. Paoli, M. A. Papa, H. R. Paris, W. Parker, D. Pascucci, A. Pasqualetti, R. Passaquieti, D. Passuello, B. Patricelli, Z. Patrick, B. L. Pearlstone, M. Pedraza, R. Pedurand, L. Pekowsky, A. Pele, S. Penn, A. Perreca, H. P. Pfeiffer, M. Phelps, O. Piccinni, M. Pichot, M. Pickenpack, F. Piergiovanni, V. Pierro, G. Pillant, L. Pinard, I. M. Pinto, M. Pitkin, J. H. Poeld, R. Poggiani, P. Popolizio, A. Post, J. Powell, J. Prasad, V. Predoi, S. S. Premachandra, T. Prestegard, L. R. Price, M. Prijatelj, M. Principe, S. Privitera, R. Prix, G. A. Prodi, L. Prokhorov, O. Puncken, M. Punturo, P. Puppo, M. Pürrer, H. Qi, J. Qin, V. Quetschke, E. A. Quintero, R. Quitzow-James, F. J. Raab, D. S. Rabeling, H. Radkins, P. Raffai, S. Raja, M. Rakhmanov, C. R. Ramet, P. Rapagnani, V. Raymond, M. Razzano, V. Re, J. Read, C. M. Reed, T. Regimbau, L. Rei, S. Reid, D. H. Reitze, H. Rew, S. D. Reyes, F. Ricci, K. Riles, N. A. Robertson, R. Robie, F. Robinet, A. Rocchi, L. Rolland, J. G. Rollins, V. J. Roma, J. D. Romano, R. Romano, G. Romanov, J. H. Romie, D. Rosińska, S. Rowan, A. Rüdiger, P. Ruggi, K. Ryan, S. Sachdev, T. Sadecki, L. Sadeghian, L. Salconi, M. Saleem, F. Salemi, A. Samajdar, L. Sammut, L. M. Sampson, E. J. Sanchez, V. Sandberg, B. Sandeen, G. H.

Sanders, J. R. Sanders, B. Sassolas, B. S. Sathyaprakash, P. R. Saulson, O. Sauter, R. L. Savage, A. Sawadsky, P. Schale, R. Schilling, J. Schmidt, P. Schmidt, R. Schnabel, R. M. S. Schofield, A. Schönbeck, E. Schreiber, D. Schuette, B. F. Schutz, J. Scott, S. M. Scott, D. Sellers, A. S. Sengupta, D. Sentenac, V. Sequino, A. Sergeev, G. Serna, Y. Setyawati, A. Sevigny, D. A. Shaddock, T. Shaffer, S. Shah, M. S. Shahriar, M. Shaltev, Z. Shao, B. Shapiro, P. Shawhan, A. Sheperd, D. H. Shoemaker, D. M. Shoemaker, K. Siellez, X. Siemens, D. Sigg, A. D. Silva, D. Simakov, A. Singer, L. P. Singer, A. Singh, R. Singh, A. Singhal, A. M. Sintes, B. J. J. Slagmolen, J. R. Smith, M. R. Smith, N. D. Smith, R. J. E. Smith, E. J. Son, B. Sorazu, F. Sorrentino, T. Souradeep, A. K. Srivastava, A. Staley, M. Steinke, J. Steinlechner, S. Steinlechner, D. Steinmeyer, B. C. Stephens, S. P. Stevenson, R. Stone, K. A. Strain, N. Straniero, G. Stratta, N. A. Strauss, S. Strigin, R. Sturani, A. L. Stuver, T. Z. Summerscales, L. Sun, P. J. Sutton, B. L. Swinkels, M. J. Szczepańczyk, M. Tacca, D. Talukder, D. B. Tanner, M. Tápai, S. P. Tarabrin, A. Taracchini, R. Taylor, T. Theeg, M. P. Thirugnanasambandam, E. G. Thomas, M. Thomas, P. Thomas, K. A. Thorne, K. S. Thorne, E. Thrane, S. Tiwari, V. Tiwari, K. V. Tokmakov, C. Tomlinson, M. Tonelli, C. V. Torres, C. I. Torrie, D. Töyrä, F. Travasso, G. Traylor, D. Trifirò, M. C. Tringali, L. Trozzo, M. Tse, M. Turconi, D. Tuyenbayev, D. Ugolini, C. S. Unnikrishnan, A. L. Urban, S. A. Usman, H. Vahlbruch, G. Vajente, G. Valdes, M. Vallisneri, N. van Bakel, M. van Beuzekom, J. F. J. van den Brand, C. Van Den Broeck, D. C. Vander-Hyde, L. van der Schaaf, J. V. van Heijningen, A. A. van Veggel, M. Vardaro, S. Vass, M. Vasúth, R. Vaulin, A. Vecchio, G. Vedovato, J. Veitch, P. J. Veitch, K. Venkateswara, D. Verkindt, F. Vetrano, A. Viceré, S. Vinciguerra, D. J. Vine, J.-Y. Vinet, S. Vitale, T. Vo, H. Vocca, C. Vorvick, D. Voss, W. D. Vousden, S. P. Vyatchanin, A. R. Wade, L. E. Wade, M. Wade, S. J. Waldman, M. Walker, L. Wallace, S. Walsh, G. Wang, H. Wang, M. Wang, X. Wang, Y. Wang, H. Ward, R. L. Ward, J. Warner, M. Was, B. Weaver, L.-W. Wei, M. Weinert, A. J. Weinstein, R. Weiss, T. Welborn, L. Wen, P. Weßels, T. Westphal, K. Wette, J. T. Whelan, S. E. Whitcomb, D. J. White, B. F. Whiting, K. Wiesner, C. Wilkinson, P. A. Willems, L. Williams, R. D. Williams, A. R. Williamson, J. L. Willis, B. Willke, M. H. Wimmer, L. Winkelmann, W. Winkler, C. C. Wipf, A. G. Wiseman, H. Wittel, G. Woan, J. Worden, J. L. Wright, G. Wu, J. Yablon, I. Yakushin, W. Yam, H. Yamamoto, C. C. Yancey, M. J. Yap, H. Yu, M. Yvert, A. Zadrożny, L. Zangrando,

M. Zanolin, J.-P. Zendri, M. Zevin, F. Zhang, L. Zhang, M. Zhang, Y. Zhang, C. Zhao, M. Zhou, Z. Zhou, X. J. Zhu, M. E. Zucker, S. E. Zuraw, and J. Zweizig. Observation of gravitational waves from a binary black hole merger. *Phys. Rev. Lett.*, 116:061102, Feb 2016.

[2] R. Arnowitt, S. Deser, and C. W. Misner. The dynamics of general relativity. *Gravitation: An Introduction to Current Research*, pages 227–265, 1962.

[3] T. W. Baumgarte and S. L. Shapiro. On the numerical integration of Einstein's field equations. *Phys. Rev.*, D59:024007, 1999.

[4] M. J. Berger and P. Colella. Local adaptive mesh refinement for shock hydrodynamics. *Journal of Computational Physics*, 82:64–84, May 1989.

[5] S. Bonazzola, E. Gourgoulhon, and J.-A. Marck. Numerical approach for high precision 3d relativistic star models. *Phys. Rev. D*, 58:104020, Oct 1998.

[6] C. Canuto, M. Hussaini, A. Quarteroni, and T. Zang. *Spectral Methods: Evolution to Complex Geometries and Application to Fluid Dynamics.* Springer Berlin Heidelburg New York, 2007.

[7] A. Einstein. Die Grundlage der allgemeinen Relativitätstheorie. *Annalen der Physik*, 354:769–822, 1916.

[8] E. Gourgoulhon, P. Grandclément, J.-A. Marck, J. Novak, and K. Taniguchi. LORENE: Spectral methods differential equations solver. Astrophysics Source Code Library, Aug. 2016.

[9] B. James. Initial Data for a Binary Black Hole System. Unpublished Thesis, 2013.

[10] F. Löffler, J. Faber, E. Bentivegna, T. Bode, P. Diener, R. Haas, I. Hinder, B. C. Mundim, C. D. Ott, E. Schnetter, G. Allen, M. Campanelli, and P. Laguna. The Einstein Toolkit: A Community Computational Infrastructure for Relativistic Astrophysics. *Class. Quantum Grav.*, 29(11):115001, 2012.

[11] C. O. Lousto and Y. Zlochower. Orbital evolution of extreme-mass-ratio black-hole binaries with numerical relativity. *Phys. Rev. Lett.*, 106:041101, Jan 2011.

[12] Marmelad, 2008. http://creativecommons.org/licenses/by-sa/3.0/deed.en.

[13] S. C. Noble, J. H. Krolik, and J. F. Hawley. Direct calculation of the radiative efficiency of an accretion disk around a black hole. *The Astrophysical Journal*, 692(1):411, 2009.

[14] E. Schnetter, 2011. http://www.carpetcode.org/.

[15] M. Shibata and T. Nakamura. Evolution of three-dimensional gravitational waves: Harmonic slicing case. *Phys. Rev. D*, 52:5428–5444, Nov 1995.